Supplementary Information

Leveraging polymer architecture design with acylamino functionalization for electrolytes to enable highly durable lithium metal batteries

Jiayu Zheng,[a] Lingyan Duan,[a]* Hang Ma,[b] Qi An,[a] Qing Liu,[a] Yongjiang Sun,[a] Genfu Zhao,[a] Hanlin Tang,[a] Li yang,[a] Shimin Wang,[a] Qijun Xu,[a] Lilian wang,[a] Hong Guo[a,c]*

[a] International Joint Research Center for Advanced Energy Materials of Yunnan Province, School of Materials and Energy, Yunnan University, Kunming 650091, China.

[b] R & D Center, Yunnan Yuntianhua Co., Ltd., Kunming 650228, China

[c] Southwest United Graduate School, Kunming 650091, China

*Corresponding Author

E-mail: Lingyan.duan@ynu.edu.cn, guohong@ynu.edu.cn

Experimental Section

Materials

Poly(hexamethylene diisocyanate) (PHDI, Sigma-Aldrich), Poly(ethylene glycol) methacrylate (PEGMA, average Mn = 360 g mol^{-1} and 500 g mol^{-1}, Sigma-Aldrich), 2-hydroxyethyl methacrylate (2-HEMA, ≥99%, Sigma-Aldrich), dibutyltin dilaurate (DBTDL, 95%+, Adamas), vinylene carbonate(VC, 98%, Adamas), α, α′-azobis(isobutyronitrile) (AIBN, 99%, Aladdin), lithium nitrate ($LiNO_3$, 99%+, Adamas), acetone (99.9%, Adamas), and anhydrous diethyl ether (≥99.7%, Greagent) were purchased from Shanghai Titan Scientific Co., Ltd. Commercial liquid carbonate electrolyte (1M $LiPF_6$ in EC: DEC = 1:1 wt%) was obtained from DodoChem Co., Ltd. Lithium iron phosphate ($LiFePO_4$, LFP), lithium cobalt oxide ($LiCoO_2$, LCO), and Ni-rich lithium cobalt-nickel manganese ($LiNi_{0.8}Co_{0.1}Mn_{0.1}O_2$, NCM811) were obtained from Hefei Kejing Material Technology Co., Ltd. Polyvinylidene fluoride (PVDF, 5130), conductive agents (Super P), and N-methyl pyrrolidone (NMP) were purchased from Guangdong Canrd New Energy Technology Co., Ltd. Unless otherwise indicated, all reagents used in this study were utilized directly without further purification.

Detailed experimental procedures of GPE fabrication

Acylamino-functionalized GPE was fabricated via in-situ radical polymerization of a uniform gel precursor solution containing crosslinker-n (n = 1, 6, 9), VC monomer, AIBN thermal initiator, commercial liquid carbonate electrolyte (1M LiPF6 in EC and DEC with a weight of 1: 1), and $LiNO_3$. The obtained GPE is denoted as GPEn-x/y, where n represents the species of crosslinker, and an additional "-x/y" indicates the molar ratio of crosslinker-n/VC, e.g., for a GPE comprising crosslinker-6 and with a crosslinker-n/VC molar ratio of 3/7, the notation is GPE6-3/7. For clarity, the process of creating GPE6-3/7 is employed as an illustration to account for the intricate experimental procedures associated with GPE. Initially, 20 wt.% of monomers (crosslinker-6 and VC in a 3:7 molar ratio), 80 wt.% of liquid electrolyte (LE), and $LiNO_3$ (1 wt.% concerning the total mass of crosslinker-n + VC + LE) were first mixed in a pellucid glass reagent bottle under continuous stirring until the solution became transparent. Then, AIBN (1 wt.% with respect to the total mass of crosslinker-n + VC) was added to the aforementioned solution, followed by vigorous stirring until it became a homogeneous and transparent solution. Thereafter, the prepared liquid precursor solution was used to assemble cells. Subsequently, the precursor solution was created and utilized for cell assembly, with an injection of 60 microliters of precursor solution into each cell. To assess the impact of precursor solution quantity on the electrochemical performance of GPE-based cells, LFP||GPE6-3/7||Li cells were also fabricated using lesser amounts of precursor solution (50 and 30 microliters, respectively). All these processes were carried out in an argon glovebox (Etelux Lab 2000) containing less than 0.1 ppm oxygen and moisture. Finally, the assembled cells were transferred to a vacuum oven and thermally treated at 60 °C for 12 hours, resulting in the formation of acylamino-functionalized GPE within the cells. Similarly, other GPEs with different molar ratios of crosslinker-n/VC (2/8, 4/6) or species of crosslinker-n (n = 1, 9) were fabricated through an analogous procedure.

Preparation of cathodes

LFP, LCO, and NCM811 cathodes were produced by slurry casting. For both LFP and LCO, active cathode material, PVDF, and conductive material (super P) were first dissolved in NMP in a weight ratio of 9:0.5:0.5. Then, the obtained slurry was coated onto aluminum foil, followed by vacuum drying at 80 °C for 3 hours and subsequently 120 °C for 12 hours. After that, the cathodes were cut into 14 mm diameter discs. The

LFP cathodes were available in two loading densities, approximately 3.9 and 9.9 mg cm^{-2}. For LCO, the cathode loading density was around 3.9 mg cm^{-2}. The same procedure was applied to make the NCM811 cathode, with active cathode material, PVDF, and super P used in an 8:1:1 weight ratio. The loading density of NCM811 on the cathode is about 3.6 mg cm^{-2}.

Cell assembly

The assembling of all cells was accomplished in argon gloveboxe (Etelux Lab 2000) (O_2, H_2O < 0.1 ppm, parts per million). Coin 2025-type cells were assembled using cathode LFP, LCO, or NCM811, lithium foil (500 μm in thickness, 15 mm in diameter), separator polypropylene (PP, Celgard 2400), and 60 μL of the GPE precursor solution mentioned above injected into the cell. After sealing the coin cell, the LFP||Li, LCO||Li, or NCM811||Li half cells were moved into an oven and heated for 12 hours at 60 °C. Similarly, the lithium-lithium (Li||Li) and lithium-stainless steel (Li||SS) asymmetrical cells were fabricated by replacing cathodes with Li foil and SS discs in a similar in-situ method. Likewise, the SS-SS symmetrical cell was manufactured by replacing Li foils with SS discs. As counterparts, liquid cells (equipped with commercial liquid carbonate electrolyte) were also assembled for performance comparison. To investigate the impact of the negative/positive capacity ratio (N/P ratio) on the electrochemical performance of batteries, a thin lithium foil with a thickness of 50 μm and two mass-loading LFP cathodes (3.9 and 9.9 mg cm^{-2}) were employed to assemble LFP||GPE6-3/7||Li cells. To investigate the impact of GPE precursor solution volume on the electrochemical performance of batteries, LFP||GPE6-3/7||Li cells were assembled with precursor solution at volumes of 60, 50, and 30 μL, respectively.

In the context of full-cell assembly, LFP||graphite batteries were fabricated by replacing Li metal electrodes with commercial graphite coated on copper foil, and the areal capacity balance (N/P) was within the range of 1.15 to 1.20.

Materials characterization

The characteristic signal variation of functional groups for PHDI, PEGMA, crosslinker, VC, and the as-fabricated GPE was investigated via a Fourier transform infrared spectrometer (FT-IR, Nicolet IS10, USA) with KBr as a diluter. The polymer molecular

structure for acylamino-functionalized GPE was also identified using nuclear magnetic resonance hydrogen spectroscopy (^{1}H NMR, BRUKE AVANCE III 400 MHz) with dimethylsulfoxide-d6 (DMSO-d6) as the solvent. A universal mechanical testing machine (Instron 5944) was employed to estimate the puncture resistance of GPE under a feeding speed of 0.5 mm min^{-1} and the tensile property of GPE at an extension rate of 5 mm min^{-1}. The morphology of cross-sectional GPE and the cycled electrodes was observed by scanning electron microscopy (SEM, AMRAY 1000B). The mechanical property at the nanoscale for GPE was measured by atomic force microscopy (AFM, Bruker Dimension Icon) and analyzed by nanoscope analysis software, with mappings visualized by ScanAsyst-air cantilevers in peak force quantitative nanomechanics (QNM) mode. Thermogravimetric analysis (TGA, SIMULANEOUS THERMAL ANALYZER(STA): ZCT-B) was adopted to evaluate the thermal stability of GPE in a heating rate of 10 °C min^{-1} under purified nitrogen from 25 °C to 400 °C. The morphology of solid electrolyte interphase (SEI) generated on the Li foil and cathode electrolyte interphase (CEI) formed on LFP after 100 cycles in LFP||Li cells was investigated by a high-resolution transmission electron microscope (HRTEM, JEM-2010). X-ray photoelectron spectroscopy (XPS, Thermo Fisher Scientific Co. Ltd., USA) with monochromatic 150 W Al Kα radiation was applied to verify the chemical composition of SEI and CEI, with corresponding XPS peaks identified by the Advantage software. The visualization of lithium dendrite growth was studied through online optical microscopy (Zoom 650, Shanghai Tuming Optical Instrument Co., Ltd.) using Li-Li symmetrical cells charged at a current density of 2 mA cm^{-2}. The dynamic evolution of functional groups in the electrolyte system during charging/discharging was monitored using in-situ Raman (RM-1000, Renishaw) and Fourier transform infrared FTIR spectra (Nicolet IS10, USA).

Electrochemical characterization of electrolytes and CR2025 half cells

All electrochemical tests for electrolytes, including electrochemical impedance spectroscopy (EIS), chronoamperometry, linear sweep voltammetry (LSV), as well as cyclic voltammetry (CV), were executed by an electrochemical workstation (Parstat 263A, AMETEK Co.) at room temperature.

Lithium-ion conductivity

The ionic conductivities of all fabricated GPEs in this work were tested by EIS of the SS||SS blocking cells within a frequency range of 10^{-1} to 10^{5} Hz with an alternating current amplitude of 10 mV. The ionic conductivity (σ) was calculated based on the EIS results and equation S1:

$$\sigma = \frac{L}{RS} \quad \text{(Equation S1)}$$

where L is the electrolyte thickness, R is the electrolyte resistance acquired from the EIS result (the intercept on the x-axis), and S is the electrode-electrolyte contact area.

Lithium-ion transference number

The lithium-ion transference number (t_{Li+}) of electrolytes was estimated through combined AC impedance and DC polarization techniques on Li||Li symmetrical cells with a polarization voltage of 10 mV. Then, t_{Li+} was calculated according to equation S2:

$$t_{Li^+} = \frac{I_s(\Delta V - I_0 R_0)}{I_0(\Delta V - I_s R_s)} \quad \text{(Equation S2)}$$

where ΔV is the polarization potential (10 mV), I_0 and I_s are the initial and steady-state currents obtained from the polarization curve, and R_0 and R_s are the initial and steady-state resistances examined through the EIS test before and after polarization. The EIS in the frequency range of 10^{-1}-10^{5} Hz was acquired before and after polarization.

Electrochemical stability window

The electrochemical stability window of electrolytes was evaluated through an LSV test on a Li||SS asymmetrical cell from open-circuit voltage to 6.0 V under a scan rate of 0.1 mV s^{-1} (vs. Li^+/Li).

Lithium-ion diffusion coefficient

The lithium-ion diffusion coefficient (D_{Li+}) was evaluated by the cyclic voltammetry (CV) method and calculated based on the Randles-Sevick equation listed in the manuscript. The CV test was performed on the LFP||GPE6-3/7||Li and LFP||LE||Li half coin cells at varying scan rates of 0.1, 0.2, 0.3, 0.4, and 0.5 mV s^{-1}.

Galvanostatic charge-discharge test

The galvanostatic charge-discharge tests for LFP||Li, LCO||Li, and NCM811||Li CR2025 half cells were conducted using a battery test system (NEWARE, CT-4008-5V50mA-164) at 30°C. The charging/discharging voltage range for LFP||Li cells was between 2.5 and 4.0 V (vs. Li/Li^+) at 1.0 C (1 C = 170 mA g^{-1}). For rate performance, the LFP||Li cells were tested at various current densities of 0.1, 0.2, 0.5, 1.0, and 2.0 C for five cycles. The LCO||Li cells were charged and discharged in a voltage range from 3.0 to 4.2 V (vs. Li/Li^+) at 1.0 C (1 C = 140 mA g^{-1}), with rate performance detected at various current densities of 0.2, 0.5, 1.0, and 2.0 C for five cycles. The cycling performance of LCO||Li cells was evaluated by charging and discharging at 1.0 C in the voltage range of 3.0 to 4.2 and 4.3 V, respectively. The NCM811||Li cells were charged and discharged between 2.7 and 4.3 V (vs. Li/Li^+) at 1.0 C (1C = 200 mA g^{-1}). The LFP||graphite full cells were subjected to testing within the voltage range of 2.5–3.8 V.

Computational investigation

The first-principle calculations for mechanism investigation relevant to Li^+ transport and interphase composition formation were carried out using the Gaussian 16 suite of programs.[1] The geometry optimization for all studied molecules in this work was performed with PBE0 functional[2] and a 6-31+G(d) basis set, followed by single point calculations with a 6-311++G(2d,p) basis set.[3] The molecular orbital levels of all studied components were investigated via density functional theory analysis, including binding energies of Li^+ or anions to the representative Acylamino & VC unit, the highest occupied molecular orbital (HOMO), and the lowest unoccupied molecular orbital (LUMO) for constituents in the GPE system, as well as the electrostatic potential (ESP) distribution for the representative Acylamino & VC unit. The SMD solvation model[4] was used throughout the calculations, and the dielectric constant of the solvent molecule (EC) was taken from the literature.[5] The ESP calculation was conducted by Multiwfn 3.8 (dev)[6] on the basis of a highly effective algorithm.[7] All figures in the manuscript were presented via Visual Molecular Dynamics[8] (VMD) 1.9.3.

Supporting Figures

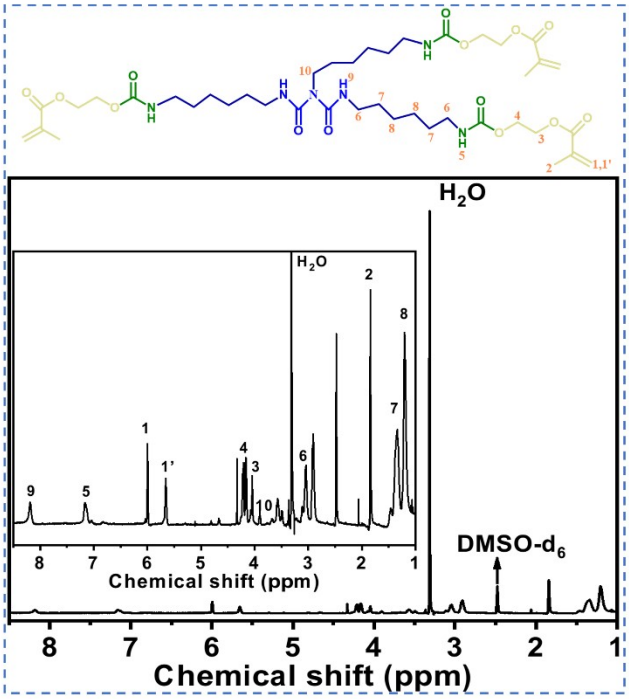

Fig. S1 Structural formula and the corresponding ^{1}H-NMR spectroscopy of crosslinker-1.

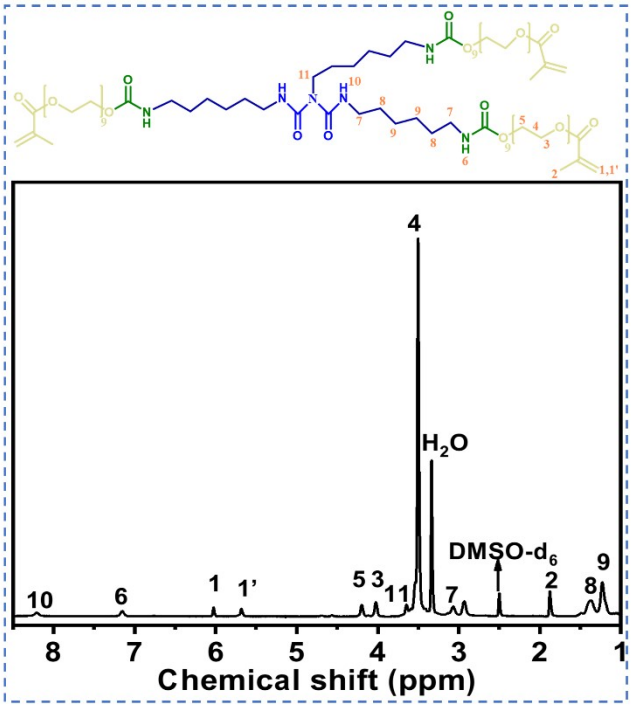

Fig. S2 Structural formula and the corresponding ^{1}H-NMR spectroscopy of crosslinker-9.

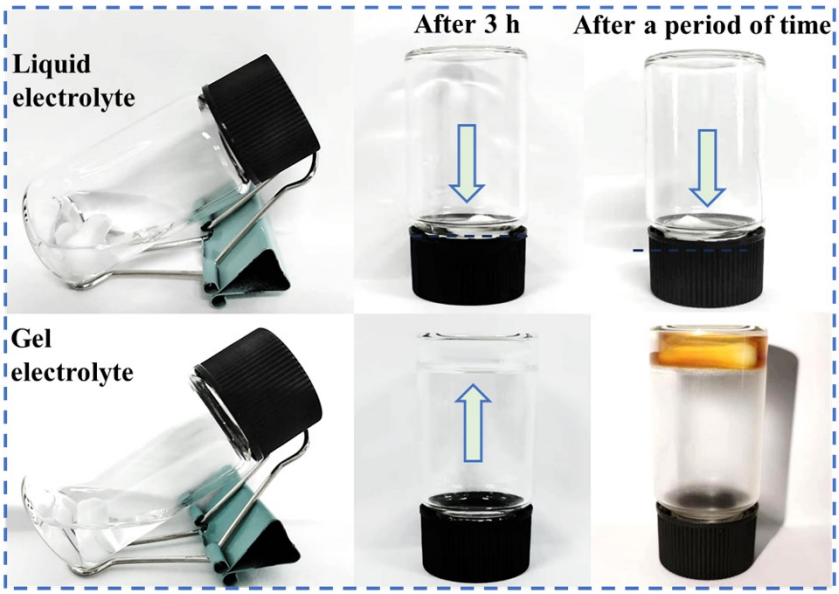

Fig. S3 Optical images of liquid electrolyte and GPE before and after polymerization.

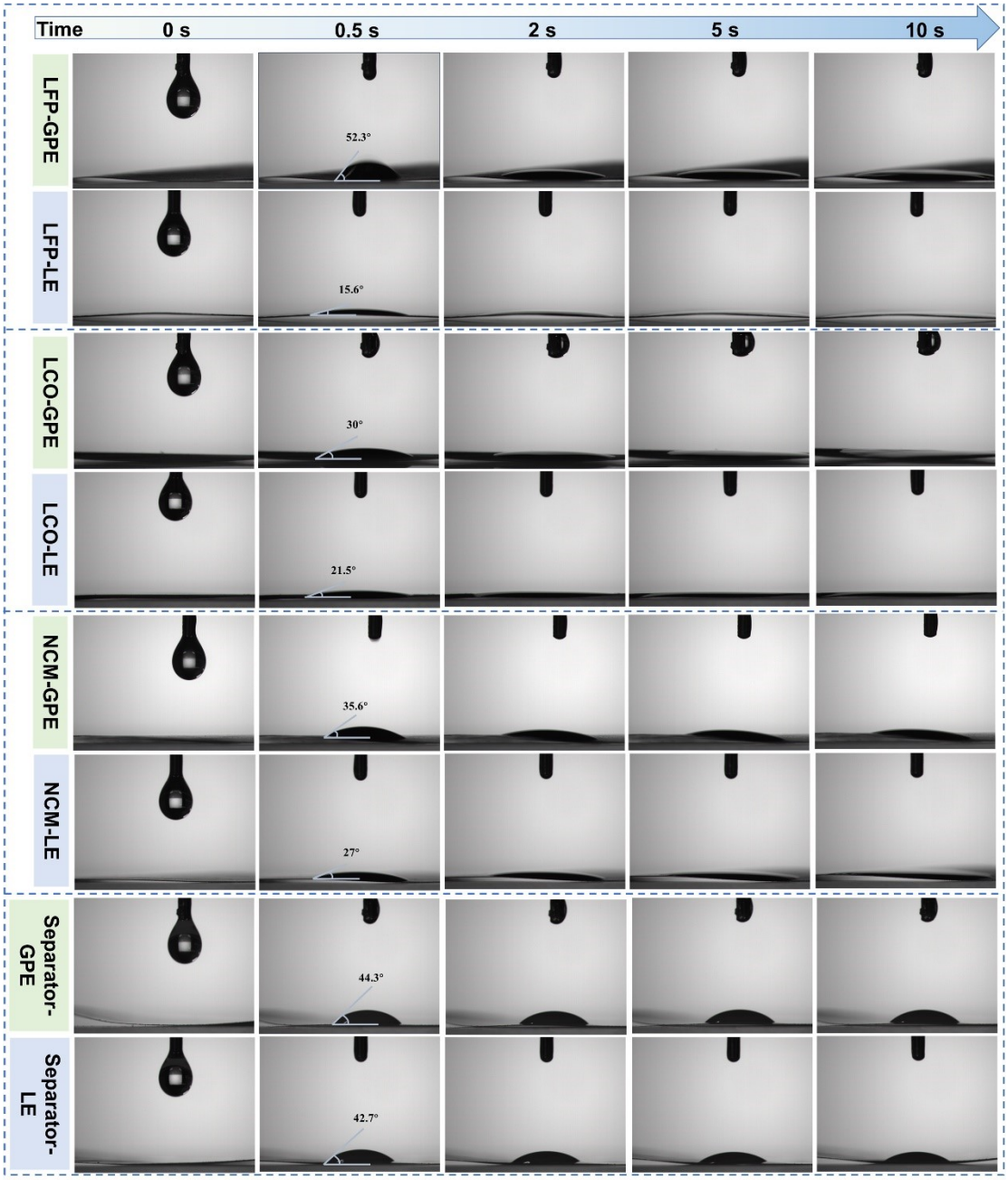

Fig. S4 Contact angle measurement of the GPE precursor solution and liquid electrolyte on different cathodes (LFP, LCO, and NCM811) and commercial Celgard separator.

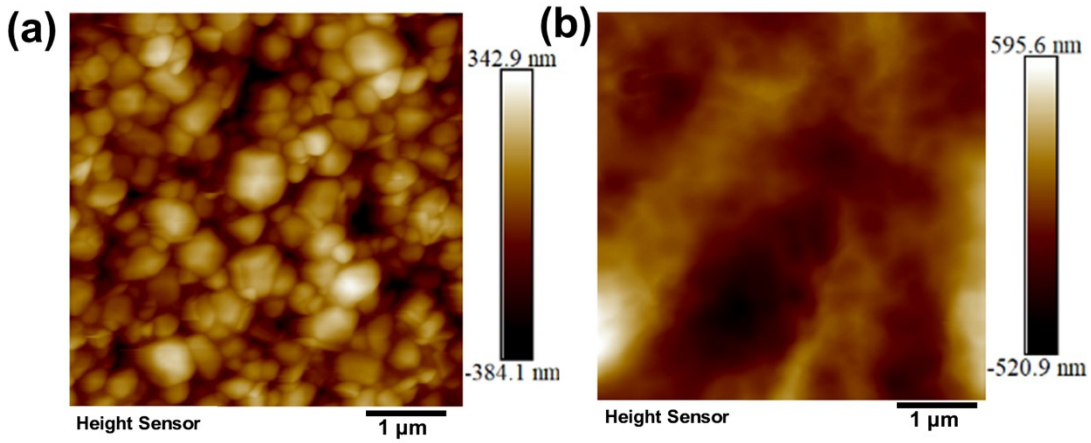

Electrolyte	(a) GPE1-3/7	(b) GPE6-3/7
Average roughness Ra/nm	82.8nm	103nm

Fig. S5 Roughness mappings of (a) GPE1-3/7 and (b) GPE6-3/7 obtained by AFM .

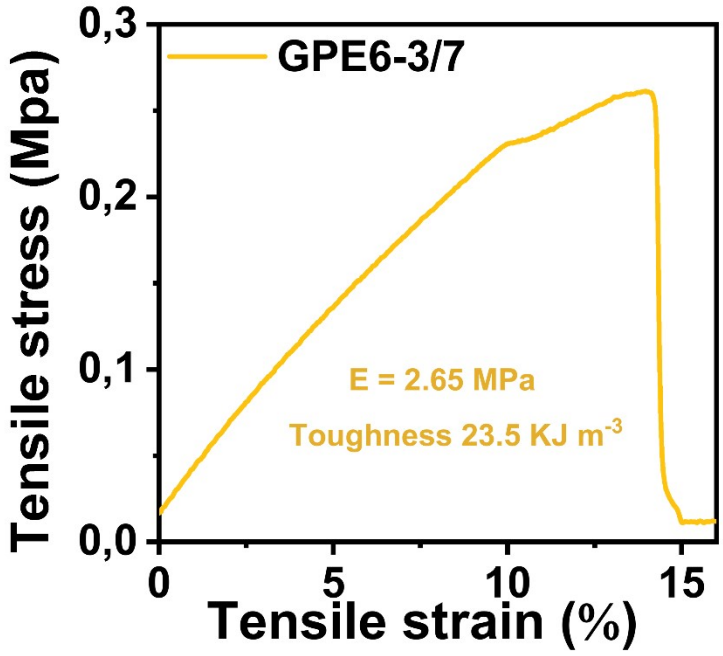

Fig. S6 Stress-strain curves of GPE6-3/7 under a stretching rate of 5 mm min^{-1}. The elastic modulus is obtained from mechanical performance testing software. The toughness value of GPE6-3/7 is determined by integrating its stress-strain curve.

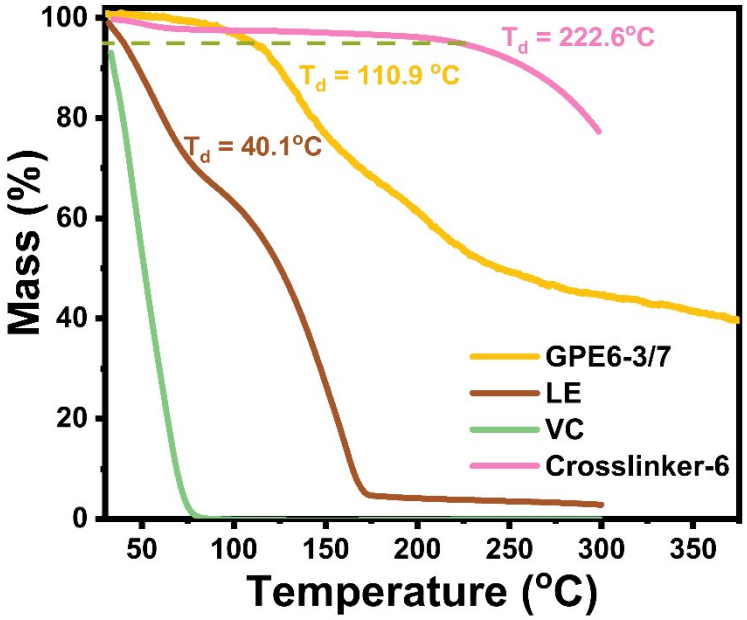

Fig. S7 Thermogravimetric analysis (TGA) curves of GPE6-3/7, LE, VC and crosslinker-6.

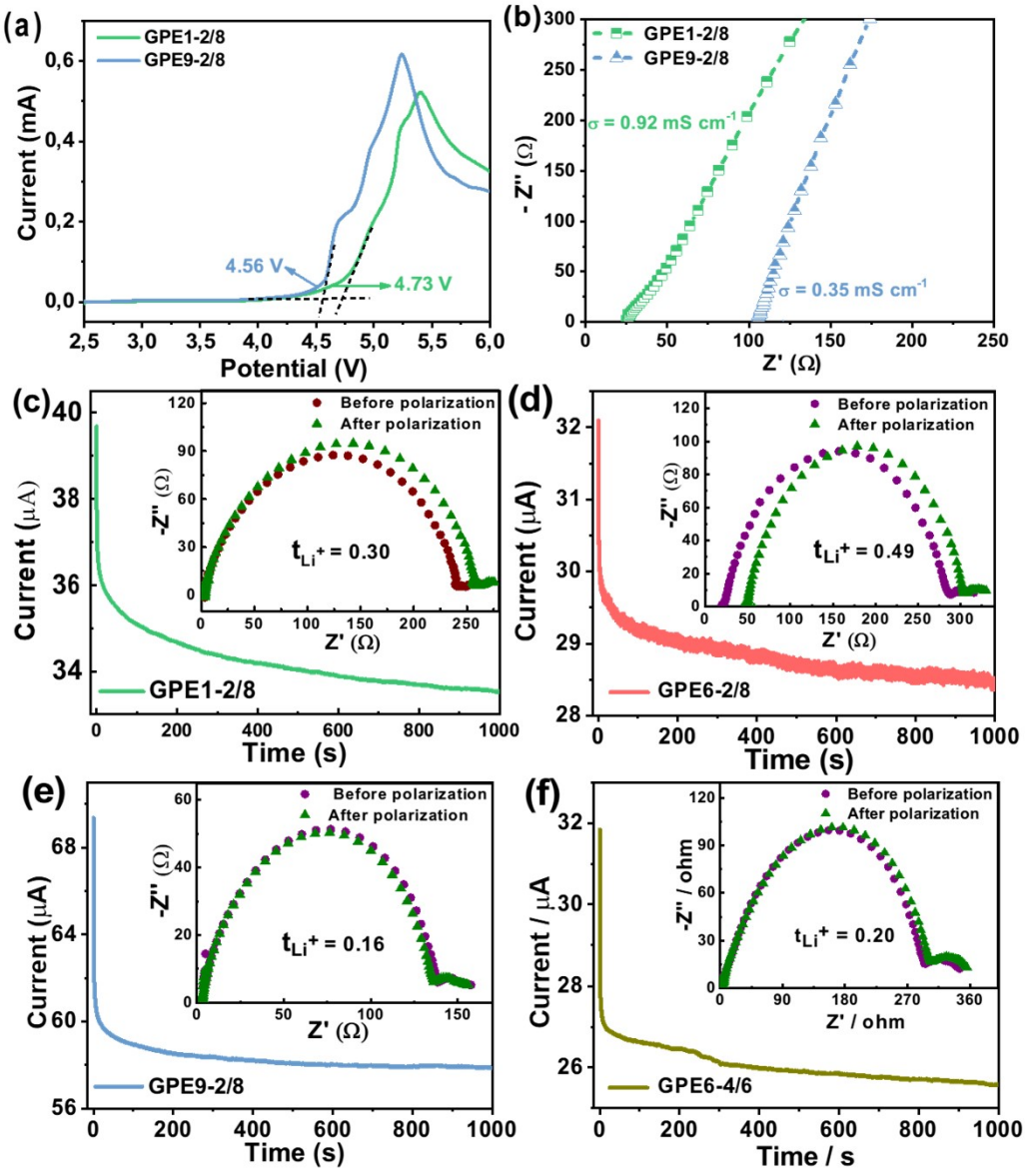

Fig. S8 (a) Linear sweep voltammetry (LSV) curves and (b) Nyquist curves at room temperature for GPE1-2/8 and GPE9-2/8. Chronoamperometry polarization curves, the impedance spectra before and after polarization (inset), and the corresponding Li^+ transfer number (t_{Li+}) (inset) of Li||Li symmetric cells paired with (c) GPE1-2/8, (d) GPE6-2/8, (e) GPE9-2/8, and (f) GPE6-4/6, respectively.

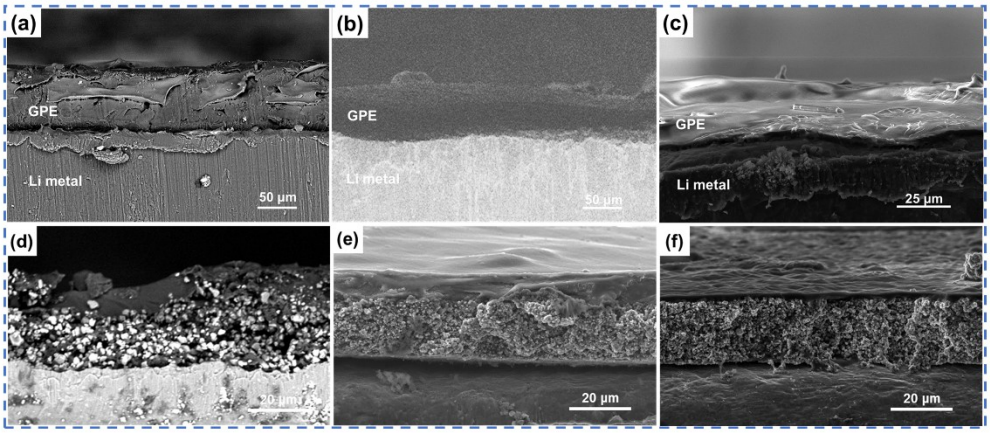

Fig. S9 Cross-sectional SEM images of (a, b, c) GPE6-3/7|Li and (d, e, f) LFP|GPE6-3/7 assembled with (a, d) 60, (b, e) 50, and (c, f) 30 μL precursor solution. The average thickness of the GPE layer on the Li metal is approximately (a) 71, (b) 54, and (c) 29 μm, respectively. The corresponding GPE layer covering the LFP cathode is approximately 10 μm thick for (d) and (e), whereas the GPE layer thickness is around 3 μm for (f).

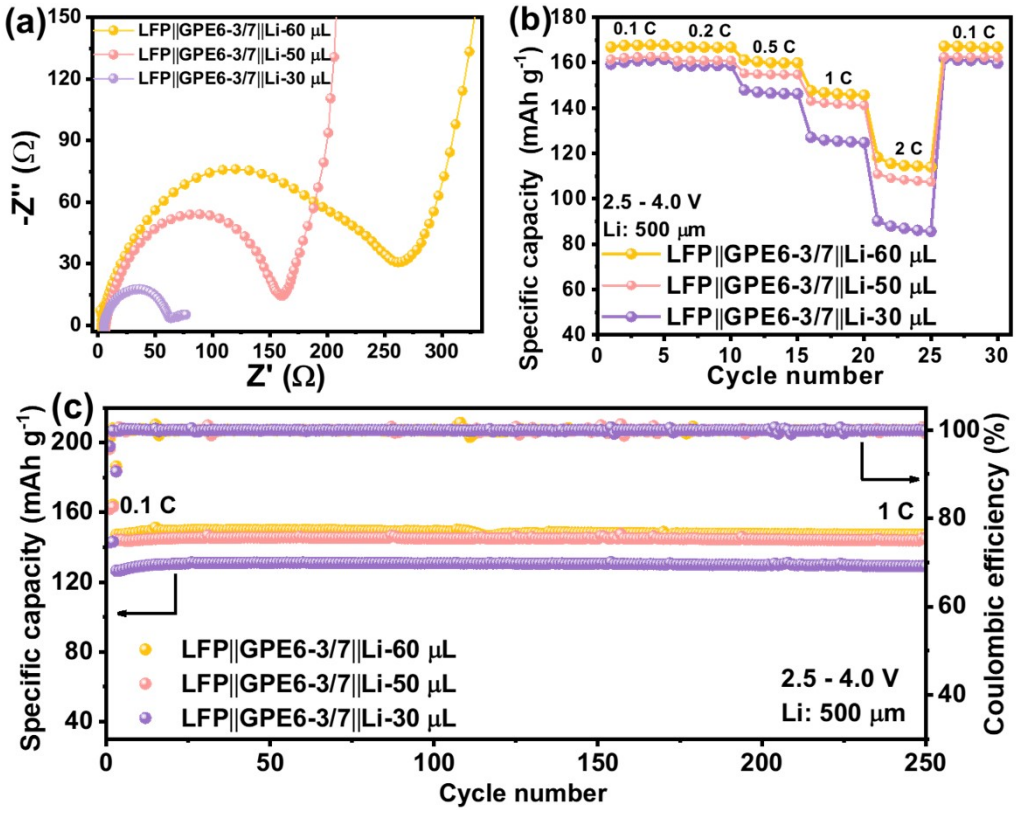

Fig. S10 The influence of the GPE precursor solution quantity on impedance and electrochemical performance of the LFP||GPE6-3/7||Li cell. (a) Electrochemical impedance spectrum. (b) Rate performances. (c) The cycling performance of the LFP||GPE6-3/7||Li cell at 1 C.

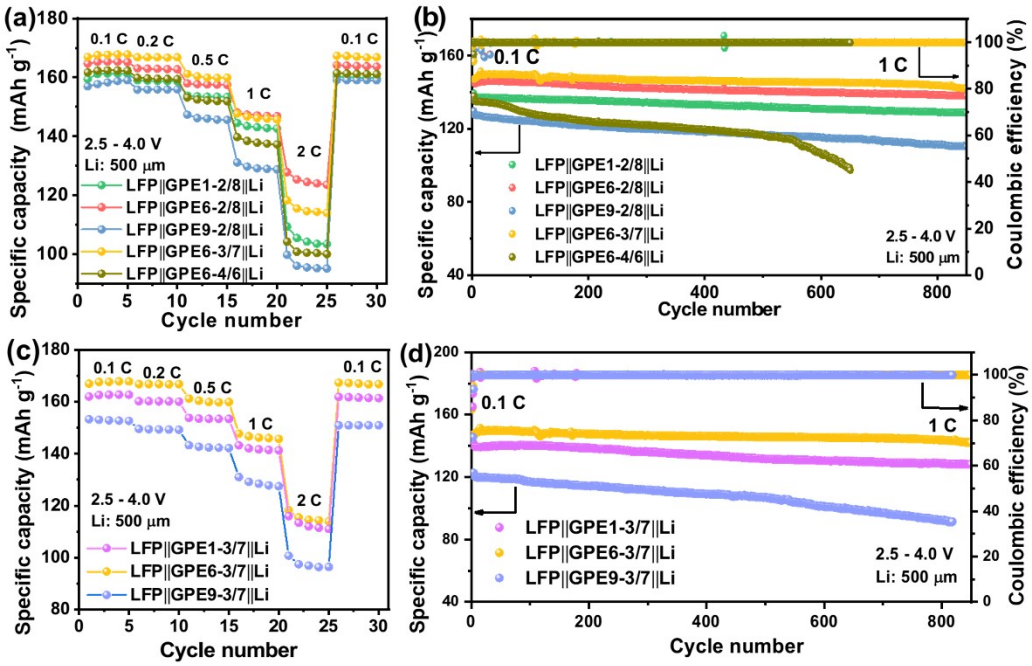

Fig. S11 (a) rate and (c) cycling performance at 1 C of LFP||GPE||Li cells assembled with GPE(1, 6, 9)-2/8, GPE6-3/7, and GPE6-6/4. (c) Rate and (d) cycling capacity at 1 C of LFP||GPE||Li cells matched with GPE(1, 6, 9)-3/7.

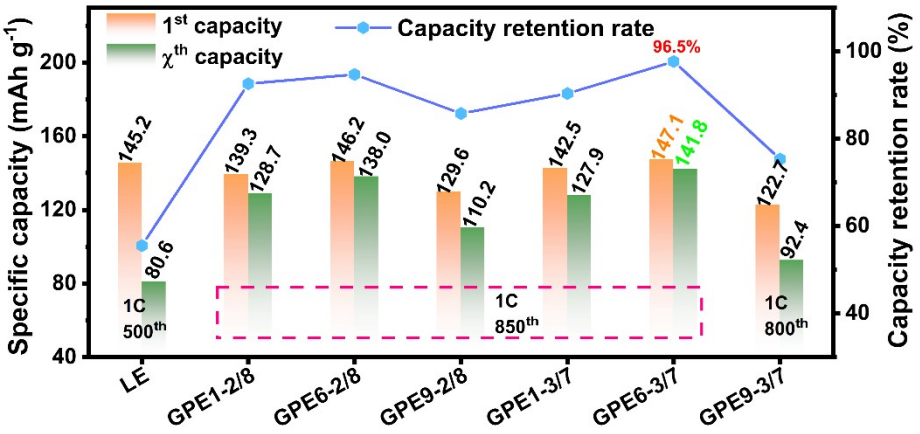

Fig. S12 Cycling performance summary regarding the specific capacity and capacity retention rate of LFP||Li cells assembled with all as-constructed GPEs in this work.

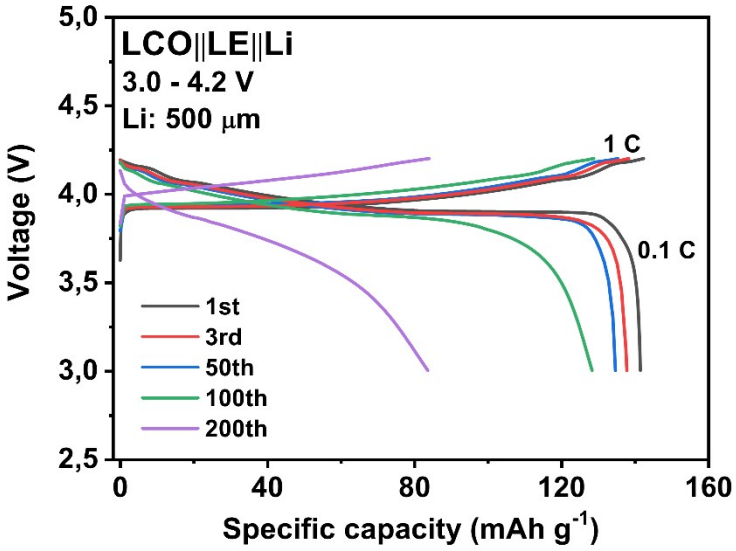

Fig. S13 The relevant Galvanostatic voltage profiles of LCO||LE||Li at various cycles.

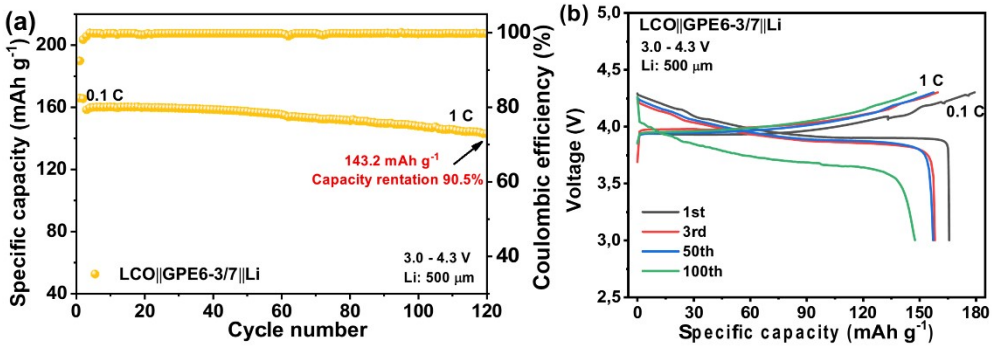

Fig. S14 (a) Cycling performance and (b) galvanostatic voltage profiles of LCO||GPE6-3/7||Li at a charging cut-off voltage of 4.3 V and 1 C.

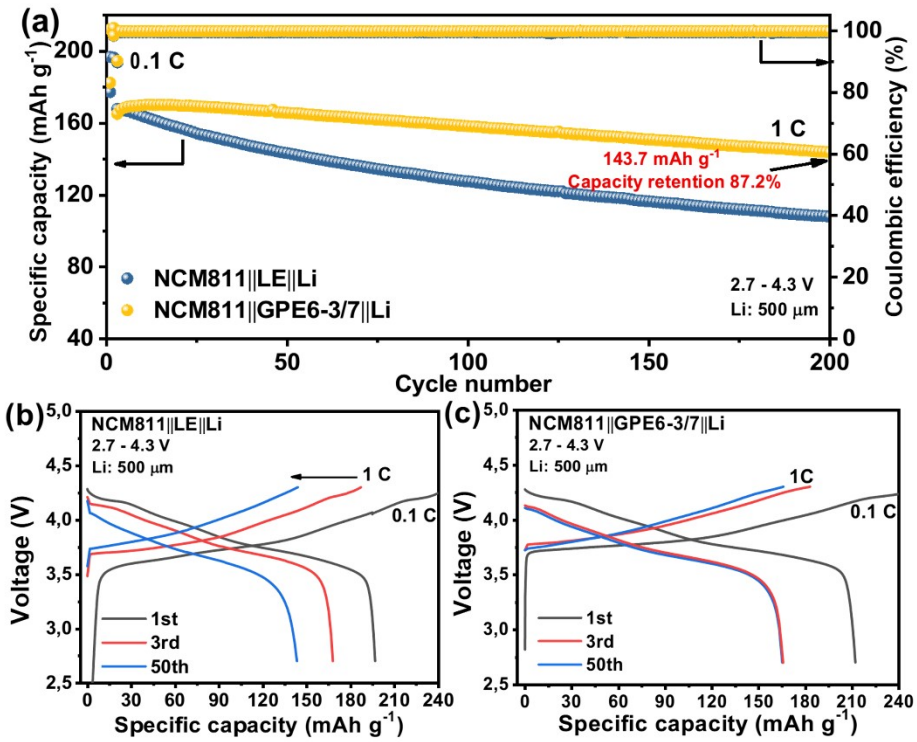

Fig. S15 (a) Cycling performance at 1 C for NCM811||LE||Li and NCM811||GPE6-3/7||Li cells. The relevant galvanostatic voltage profiles of (b) NCM811||LE||Li and (c) NCM811||GPE6-3/7||Li at various cycles.

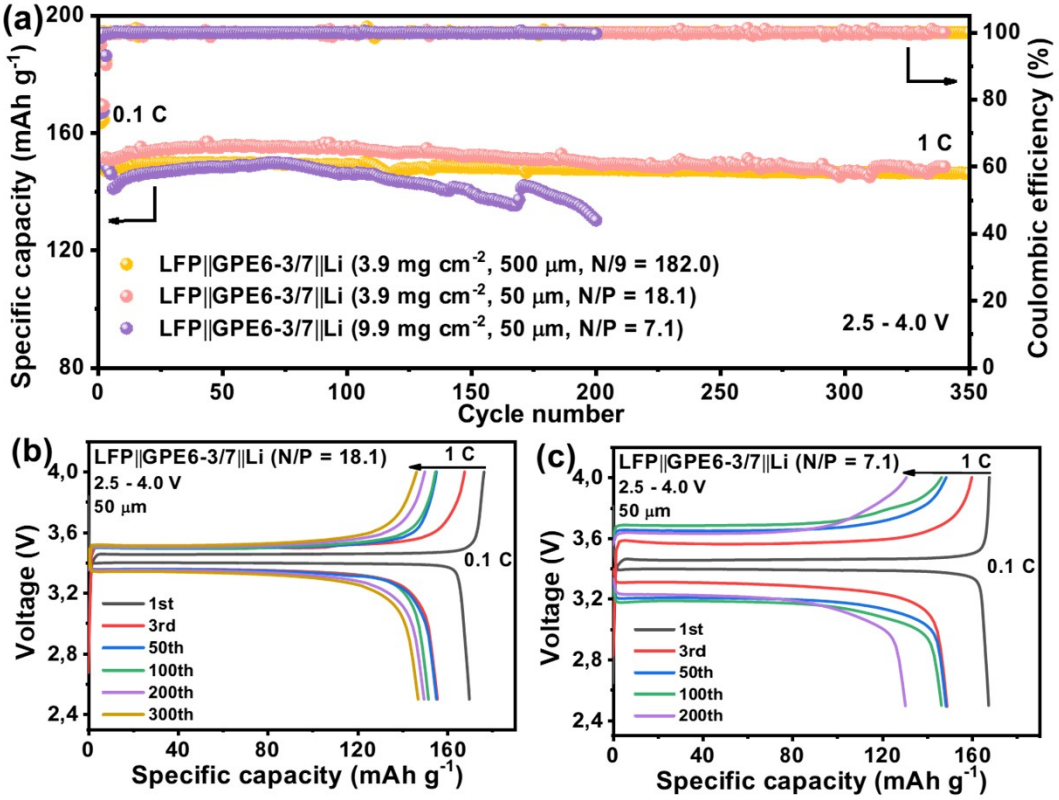

Fig. S16 (a) Cycling performances of the LFP||GPE6/3-7||Li cell with lower N/P ratios of 18.1 and 7.1. (b, c) Galvanostatic voltage profiles of LFP||GPE6/3-7||Li with different N/P ratio at various cycles.

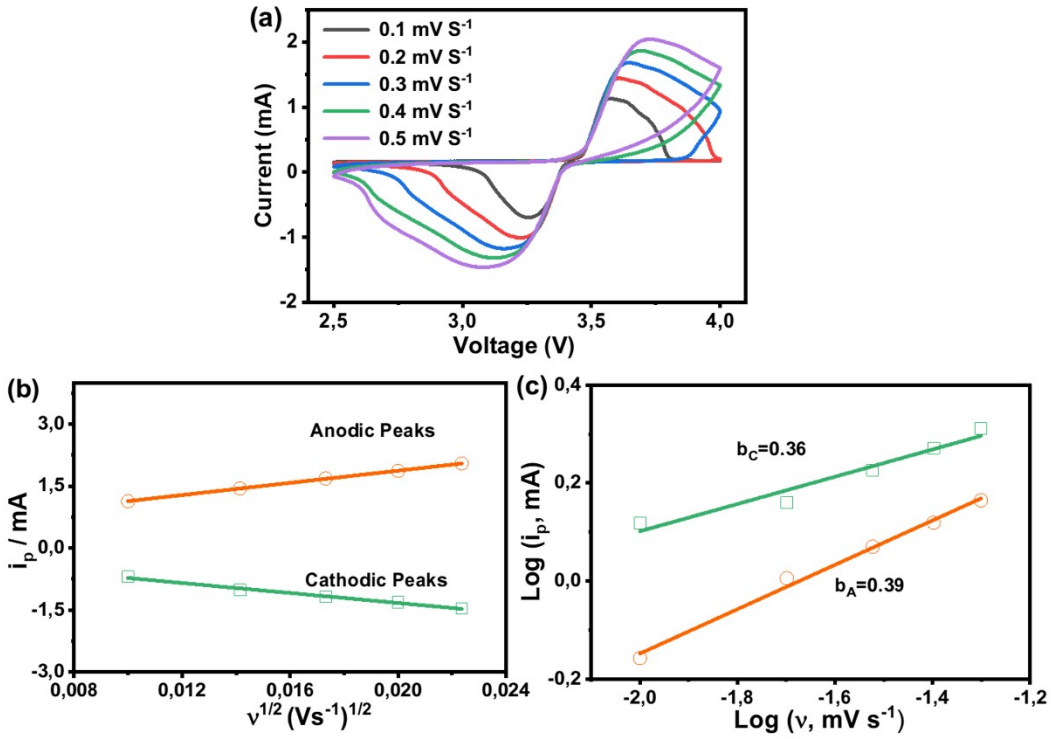

Fig. S17 (a) CV curves of LFP||LE||Li tested at various scan rates. (b) The linear fitting plots of i_p versus $v^{1/2}$. (c) The linear fitting plots of log(i_p) versus log(v).

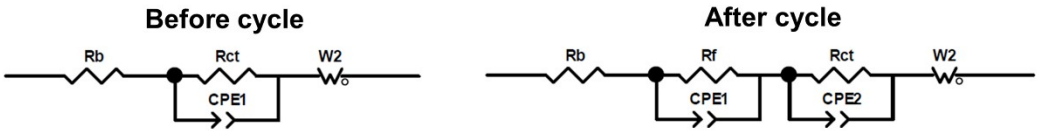

Fitting Results

		LFP||LE||Li	LFP||GPE6-3/7||Li
Before cycle	R_b	1.523	1.814
	R_{ct}	106.2	222.4
After 100 cycle	R_b	2.282	1.398
	R_f	70.86	59.9
	R_{ct}	160.2	120.1

Fig. S18 The equivalent circuits of LFP||LE||Li and LFP||GPE6-3/7||Li cells before and after 100 cycles test.

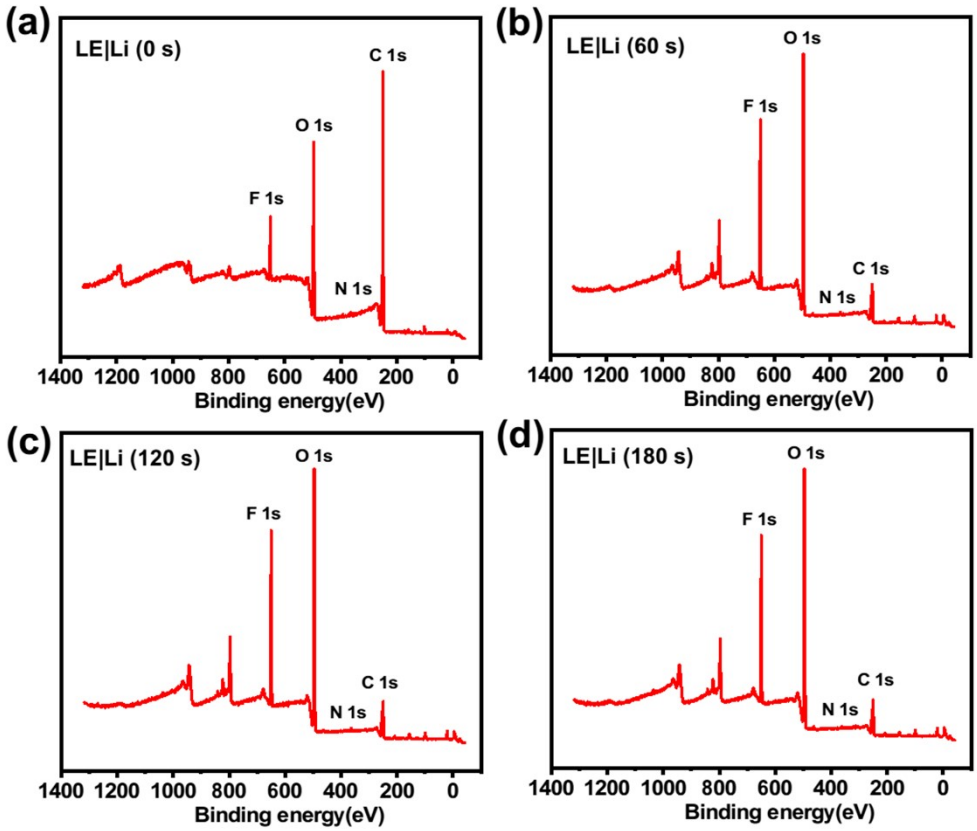

Fig. S19 Full spectrum of anode interface with increased sputtering depth of cycled LFP||LE||Li after 100 cycles.

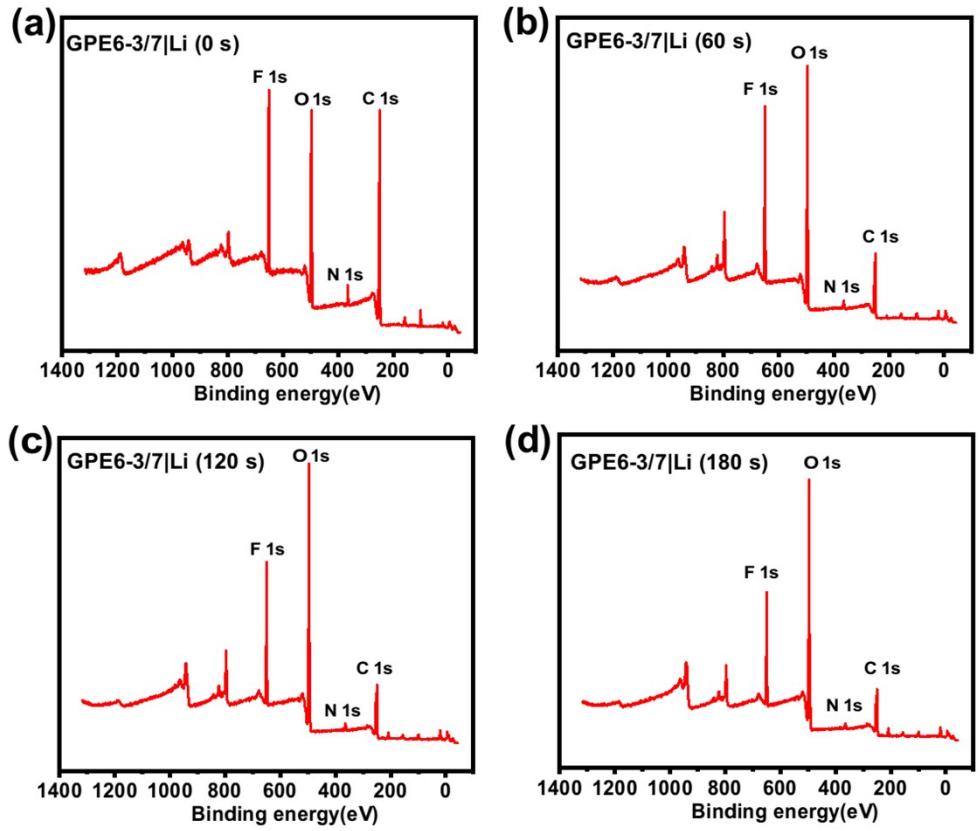

Fig. S20 Full spectrum of anode interface with increased sputtering depth of cycled LFP||GPE6-3/7||Li after 100 cycles.

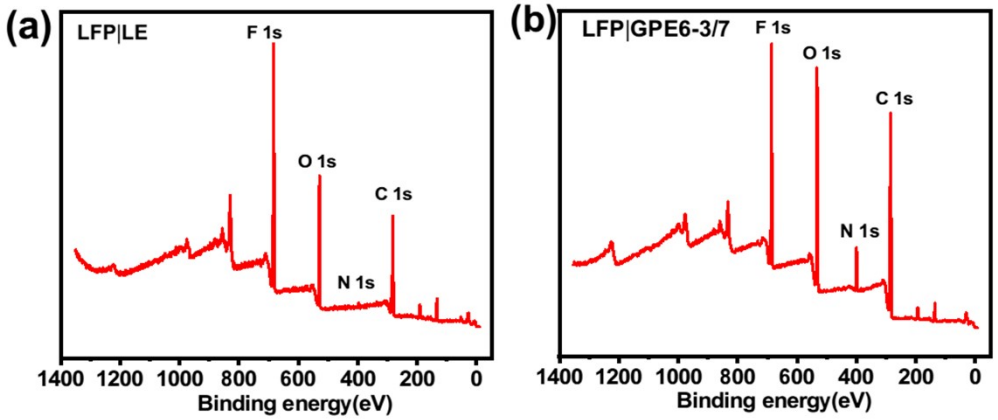

Fig. S21 Full spectrum of cathode interface of cycled (a) LFP||LE||Li and (b) LFP||GPE6-3/7||Li cells after 100 cycles.

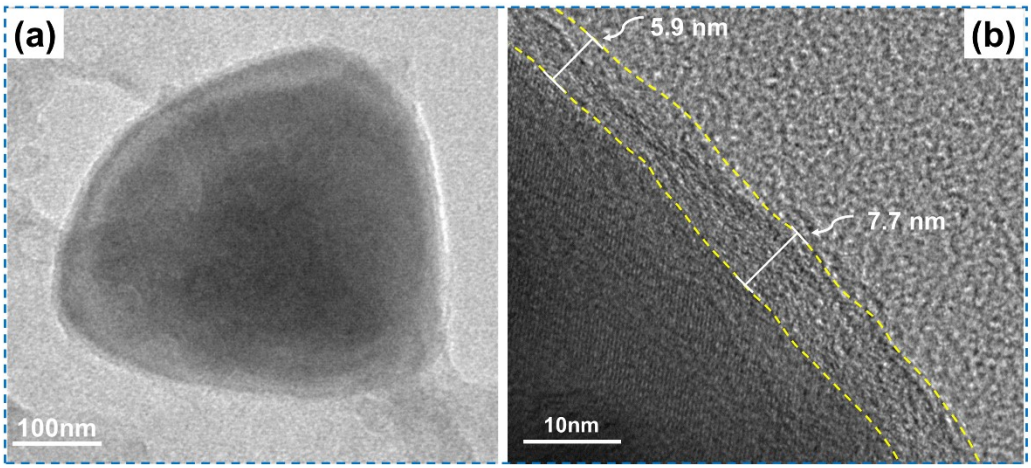

Fig. S22 TEM images of cycled LFP cathode in LFP||GPE6-3/7||Li after 100 cycles.

Table S1 Cycling performance of LFP||Li cells assembled with GPE6-3/7 in this work and some other GPEs reported recently.

Gel polymer Electrolytes	Current density (C)	Initial capacity (mAh g^{-1})	Cycle number	Capacity retention	LFP load (mg cm^{-2})	Ref.
PFVS	1	147	600	94.4%	2.8	9
PLF@GPE	0.5	150	500	91.4%	3.9	10
MOFs–GPE	1	153.1	500	98.1%	3.8	11
HCPE	1	148.9	300	88.9%	1.2	12
AGPE	0.2	161.9	150	92%	3	13
Li@MOF/Li-IL	0.5	117	500	90%	1	14
GPE	0.5	133	200	77.2%	2.5	15
GPE6-3/7	**1**	**147.1**	**850**	**96.5%**	**3.9**	**This work**

Reference

1 M. J. Frisch, G. W. Trucks, H. B. Schlegel, et al., Gaussian 16 Revision. A.03, Gaussian Inc., Wallingford, CT, 2016.

2 C. Adamo and V. Barone, *J. Chem. Phys.*, 1999, **110**, 6158–6170.

3 R. Krishnan, J. S. Binkley, R. Seeger and J. A. Pople, *J. Chem. Phys.*, 1980, **72**, 650–654.

4 A. V Marenich, C. J. Cramer and D. G. Truhlar, *J. Phys. Chem. B*, 2009, **113**, 6378–6396.

5 D. S. Hall, J. Self and J. R. Dahn, *J. Phys. Chem. C*, 2015, **119**, 22322–22330.

6 T. Lu and F. Chen, *J. Comput. Chem.*, 2012, **33**, 580–592.

7 J. Zhang and T. Lu, *Phys. Chem. Chem. Phys.*, 2021, **23**, 20323–20328.

8 W. Humphrey, A. Dalke and K. Schulten, *J. Mol. Graph.*, 1996, **14**, 33–38.

9 H. Peng, T. R. Long, J. Peng, H. Chen, L. F. Ji, H. Sun, L. Huang and S.-G. Sun, *Adv. Energy Mater.,* 2024, 2400428.

10 J. R. Gou, Z. Zhang, S. Q. Wang, J. L. Huang, K. X. Cui and H. H. Wang, *Adv. Mater.*, 2023, **2309677**, 1–10.

11 Q. Liu, L. Yang, Z. Y. Mei, Q. An, K. Zeng, W. J. Huang, S. M. Wang, Y. J. Sun and H. Guo, *Energy Environ. Sci.*, 2024, **17**, 780–790.

12 K. X. Mu, D. Wang, W. L. Dong, Q. Liu, Z. N. Song, W. J. Xu, P. P. Yao, Y. A. Chen, B. Yang, C. H. Li, L. Tian, C. Z. Zhu and J. Xu, *Adv. Mater.*, 2023, **35**, 2304686.

13 C. Ou, S. Y. Ye, Z. J. Li, X. Y. Zheng, F. Tian, D. N. Lei and C. X. Wang, *Energy Storage Mater.*, 2024, **67**, 103277.

14 P. P. Dong, X. H. Zhang, W. Hiscox, J. J. Liu, J. Zamora, X. Y. Li, M. Q. Su, Q. Zhang, X. F. Guo, J. McCloy and M.-K. Song, *Adv. Mater.*, 2023, **35**, 2211841.

15 J. Q. Zhu, H. Su, X. Han, D. Z. Zhang, J. R. Li, Y. Zhong, X. X. Xia, X. L. Wang and J. P. Tu, *Adv. Funct. Mater.*, 2023, **33**, 2302229.